Article

Ion solvation kinetics in bipolar membranes and at electrolyte–metal interfaces

Carlos G. Rodellar ⬤ , José M. Gisbert-Gonzalez, Francisco Sarabia ⬤ ,
Beatriz Roldan Cuenya ⬤ & Sebastian Z. Oener ⬤ ✉

Ion (de)solvation at solid–electrolyte interfaces is pivotal for energy and chemical conversion technology, such as (electro)catalysis, batteries and bipolar membranes. For example, during the electrocatalytic hydrogen evolution reaction in alkaline media, water needs to be dissociated and hydroxide ions solvated—a process that is not well understood. Here we study water dissociation and ion solvation kinetics in isolation at polymeric bipolar membrane and electrolyte–metal interfaces. We discover bias-dependent relationships between the activation entropy and enthalpy, which we link to a bias-dependent dispersion of interfacial capacitance. Furthermore, our results indicate that OH^- solvation is kinetically slower than H^+ solvation and that the solvation kinetics display characteristics that are independent of the catalyst structure. We attribute this to a universal amount of excess charge needed to induce electric fields that alter the interfacial entropy of water. Of fundamental interest, these results are critical to enable knowledge-driven bipolar membrane and electrocatalyst design.

Interfacial ion (de)solvation occurs whenever an ion needs to shed or gain its shell of dipolar solvents at a charged interface in bio- or electrochemistry. Conversely, every single electrocatalyst in aqueous media needs to extract or inject solvated protons or hydroxides from or to the aqueous electrolyte, whether in H_2O or CO_2 electrolysers or H_2 fuel cells. However, the solvation kinetics of protons or hydroxide ions are not understood, let alone how they compare to solvation kinetics of other charged reactants and products, including metal ions from catalyst corrosion. Conversely, current understanding of catalyst activity, selectivity and stability neglects interfacial solvation kinetics, limiting knowledge-driven development of new energy conversion technology.

In electrocatalysis, the key question is dealing with the many ways the applied electrochemical bias manifests itself across the reactive solid–electrolyte interface. Traditionally, the electrocatalyst and electrolyte structure were assumed constant under bias. For example, to address interfacial H^+ desolvation during the hydrogen evolution reaction (HER), density functional theory has been used to describe equilibrium 2D free energy surfaces dependent on the degree of solvation and distance from the (static) solid–electrolyte interface[1]. Under bias, the free enthalpy of the solvated proton is simply shifted by the applied bias. As noted by the same authors, this theory is incomplete

when part of the bias (reversibly) builds-up interfacial capacitive charge that could induce water reorientation during the solvation transition state[2]. Recently, it has been shown[3,4] that attractive ion surface interactions[5] and bias-dependent water reorganization[4,6] are critical to understand complex double layer electrostatics. However, it remains unclear how interfacial capacitance impacts (de)solvation at Faradaic turn-over.

Bias-dependent capacitance also plays a crucial role for structural catalyst dynamics, as revealed by operando catalyst spectroscopy[7–10]. Complete redox transitions lead to substantial atomic restructuring but, in completion, result in interfacial discharge. In contrast, incomplete (frustrated) phase transitions induce non-equilibrium chemical potentials and charging. As outlined before[11], the discharged class is important to understand the initial and final redox states, whereas the charged class is probably generating the key transition states during the oxygen evolution reaction—and in (bio)catalysis in general[12,13]. However, it remains unclear how interfacial capacitive excess charge impacts interfacial water dynamics, due to very limited operando solvent spectroscopy datasets[14].

Interfacial H^+ and OH^- solvation can be studied in isolation on metal (oxide) catalysts in bipolar membranes (BPMs) that spatially
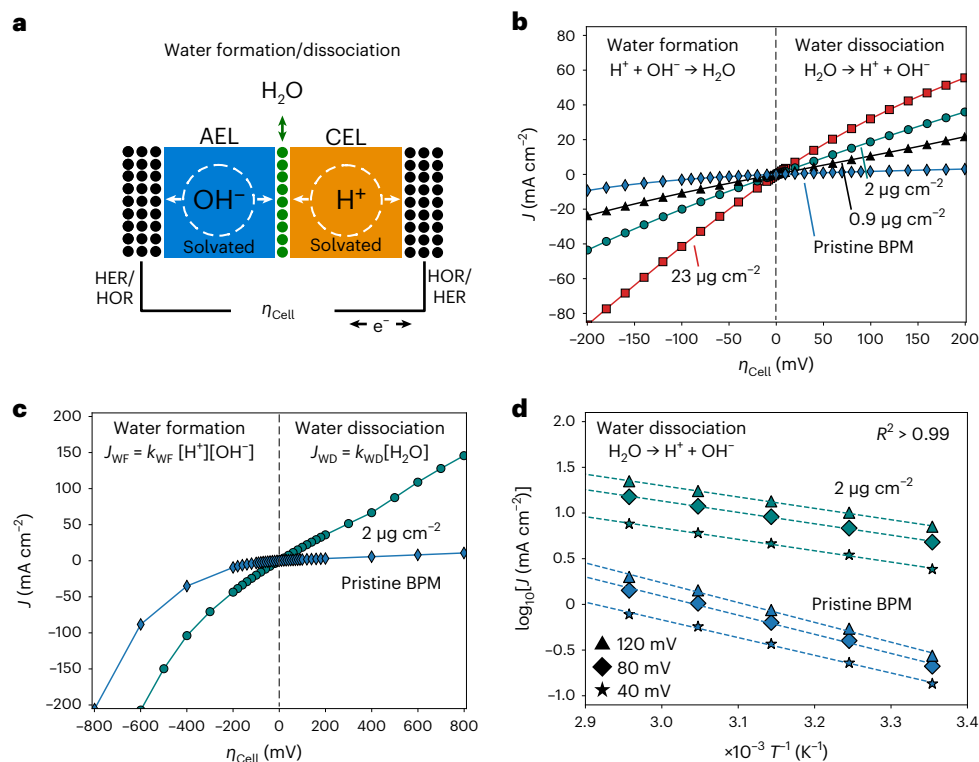
Department of Interface Science, Fritz-Haber Institute of the Max Planck Society, Berlin, Germany. ✉e-mail: oener@fhi-berlin.mpg.de

Fig. 1 | Ion (de)solvation during BPM water dissociation and water formation. **a**, The cell overpotential η_{Cell} of a H_2^{1bar}|Pt/C|BPM|Pt/C|H_2^{1bar} fuel cell/H_2 pump with 2 mg cm^{-2} HER/HOR Pt/C electrodes informing on the WD and WF kinetics of 0–15 µg cm^{-2} catalyst (SiO$_2$, TiO$_2$, HfO$_2$, CeO$_2$, IrO$_x$) loadings (green) in the BPM. **b**, Increasing TiO$_2$ loading increases WD and WF current densities (J), consistent with microscopic reversibility. **c**, At higher bias, rectifying current–voltage (I–V) behaviour is caused by bias-dependent [H$^+$] and [OH$^-$] for the forward WF rate compared to constant [H$_2$O] for the reverse WD rate. **d**, Arrhenius analysis provides the pre-exponential factor and activation energy for varying TiO$_2$ loading and potential. The dashed lines show the least-squares fit for three exemplary potentials with $R^2 > 0.99$.

isolate heterolytic water dissociation (WD; $H_2O \leftrightarrow H^+ + OH^-$) at the interface between two H$^+$ and OH$^-$ selective polymer membranes[15]. Previously, some of us observed a correlation between BPM and electrocatalyst activity for metal (oxide) catalysts, implying a fundamental link between the two fields[15]. However, a comprehensive picture about non-equilibrium electrostatics and acid–base chemistry during WD and ion (de)solvation did not emerge. Besides fundamental interest, BPMs are employed industrially in electrodialysis. Their local pH control and selective ion flow could enable H$_2$O electrolysers and H$_2$ fuel cells with better Earth-abundant catalyst activity and durability[15–18], CO$_2$ electrolysers preventing bicarbonate crossover and providing ideal product selectivity[19] and electrochemical CO$_2$ capture[20,21], among others. Despite tremendous application potential, a clear understanding of BPM function is absent—over 65 years after their invention[22].

Here we study ion solvation in isolation at polymeric BPM and electrolyte–metal junctions and when coupled with electron transfer in electrocatalysis. We discover distinct relationships between the pre-exponential factor (activation entropy) and activation energy (activation enthalpy) that are rooted in interfacial capacitance at different timescales. Our results indicate that the kinetics of OH$^-$ (de) solvation are slower than for H$^+$ (de)solvation and that there exists a universal amount of capacitive charge needed to induce electric fields that impact the interfacial entropy of water.

Surface configurational entropy–enthalpy compensation

To determine the pre-exponential factor, A, and activation energy, E_A, for ion (de)solvation, we use a H$_2$–H$_2$ BPM fuel cell/H$_2$ pump that operates the HER and hydrogen oxidation reaction (HOR) reversibly on ~2 mg cm^{-2} Pt/C electrodes. Temperature-dependent kinetics are

extracted by controlling the gas flow, temperature, back pressure and humidification from 25 °C to 75 °C. The BPM consist of a (25 µm) polymeric anion exchange layer (AEL) with fixed cationic groups and mobile OH$^-$ and a (50 µm) polymeric cation exchange layer (CEL) with fixed anionic groups and mobile H$^+$. Interfacial WD and water formation (WF) are driven at the (AEL|CEL) junction in absence (pristine BPM) and with low metal oxide catalyst loadings (0–15 µg cm^{-2}) (Fig. 1a). Methods and Supplementary Fig. 1 provide more details. Due to fast HER/HOR kinetics and two orders of magnitude dissimilar catalyst loadings, the cell overpotential informs directly on the (de)solvation kinetics inside the junction (Supplementary Fig. 2). For potentials $-0.2\,V \le \eta \le 0.2\,V$, larger metal oxide loadings increase WD and WF currents symmetrically (Fig. 1b), consistent with microscopic reversibility and a recent report by Mitchell et al.[23]. For larger potentials, rectifying behaviour emerges (Fig. 1c). In forward direction (ionic recombination), increasing [H$^+$] and [OH$^-$] increase WF currents $j_{WF} = [H^+][OH^-]k_{WF}$ with the water formation rate constant (k_{WF}) faster than WD currents in the reverse direction (ion generation), where [H$_2$O] is constant for the current densities and membrane thickness studied[18,24]. As a result, the WD current $j_{WD} = [H_2O]k_{WD}$ with the water dissociation rate constant (k_{WD}) informs on

$$k_{WD} = A(\eta) \times \exp\left(-\frac{E_A(\eta)}{k_B T}\right) \quad (1)$$

according to a first order (electro)chemical reaction following an Arrhenius rate law with the temperature T and the Boltzmann constant k_B. The latter has its statistical mechanics foundation in the Eyring–Evans–Polanyi equation[25], which links A to the activation entropy and E_A to the activation enthalpy. Despite their importance, experimental studies providing bias-dependent E_A and A are rare in electrochemistry[26].

Here we determine $E_A(\eta)$ and $A(\eta)$ with $R^2 > 0.95$ for all Arrhenius fits $\geq \pm 40$ mV (Fig. 1d and Supplementary Figs. 3 and 4).

Across different metal oxides at 40 mV and thus close to equilibrium, we observe that a high (low) E_A is compensated by a high (low) A (Fig. 2a). Here E_A and A only partially compensate, as the slope of the purple line (0.110 mol kJ^{-1}) is lower than the slope of the iso-current line (~0.154 mol kJ^{-1} at 65 °C). Apparent compensation effects (Constable−Cremer relationships) have been traditionally studied in thermal catalysis[27,28]. There, A has been separated[28] into the reduction of surface configurational, ΔS_{config}, and thermal entropy, ΔS_t, upon adsorption of a reactant onto the surface where R is the universal gas constant

$$A\left(\Delta S_{config}, \Delta S_t\right) = \exp\left(\frac{\Delta S_{config} + \Delta S_t}{R}\right) \quad (2)$$

The reduction of the surface configurational entropy can be related to the fraction of free sites Θ^*. With the exception of IrO$_x$ (more below), we find that E_A and A increase with the point of zero charge (SiO$_2 \approx 2.8$, IrO$_2 \approx 3.3$, P25-TiO$_2 \approx 6.8$, HfO$_2 \approx 7.4$, CeO$_2 \approx 8.1$) and thus in relation to the metal oxide's work function[29]. If the local pH matches the oxide's point of zero charge, the surface is at a state of maximum entropy (compare to a solvent at the potential of maximum entropy[30–32]), which can be considered as 50% coverage of all available sites, for example, all the basic sites (b-O$^-$) are covered (b-OH) and none of the acidic sites (a-OH) that could still accept a proton. However, the further the surface is away from the point of zero charge, the larger the reduction upon adsorption of a free site (Supplementary Fig. 5). Thus, A and E_A increase with the difference between local pH and point of zero charge. This trend implies that the oxides equilibrium A and E_A are primarily determined by their individual work function (related to point of zero charge) and the local pH of the acidic CEL. Supplementary Note 2 provides a full discussion, including the proposed acid–base mechanism and the electrostatic link between configurational surface and water entropy. Finally, we hypothesize that the point of zero charge range studied here leads to negligible activity at the alkaline AEL, in contrast to a previous study by some of us which included more basic oxides (point of zero charge -10–14)[15]. Regardless, the equilibrium A and E_A fall far short in describing interfacial (de)solvation comprehensively.

Bias-dependent changes of the pre-exponential factor

At applied bias, we observe a constant E_A while $A(\eta)$ is increasing (vertical arrows in Fig. 2a), consistent with a recent report for a single P25-TiO$_2$ catalyst[33]. The equilibrium E_A and A are set by the oxide properties (for example, point of zero charge) and a constant E_A thus implies a constant surface configurational entropy. We conclude that the non-conductive metal oxides remain unpolarized and electrostatically decoupled ($\epsilon \approx 2$–50) from the non-equilibrium electric fields across the junction. The latter arise from the membrane space charge regions which have a low intrinsic activity themselves (pristine BPM in Fig. 1b).

According to transition state theory, the pre-exponential factor is given by the difference in entropy between the reactant and the transition state, which includes translational, rotational and vibrational contributions, all of which could change with bias. In heterogeneous gas phase catalysis and in absence of an electrochemical bias, the pre-factor is separated into surface configurational entropy (discussed above) and thermal entropy reduction, $\Delta S_t(\nu)$, with the attempt frequency ν, which is related to the vibrational entropy reduction between the transition and initial states, and the loss of translational freedom for a molecule adsorbing onto the surface from the gas[28,34]. ΔS_t is usually considered to vary only slightly between different materials[34]. However, here the non-equilibrium electric fields across the bipolar junction[35] might impact the vibrational frequencies of the water dipoles directly. Besides thermal entropy, the electric fields might also change the configurational entropy of the water dipoles. For (homogeneous)

protolytic equilibria in aqueous solutions, auto-dissociation involves a large configurational entropy change in the water network[36]. Due to the aforementioned challenges, neither operando water spectroscopy nor theory have been able to clearly dissect the different enthalpic and entropic contributions in the inner sphere so far. Our results show that entropic contributions are critical to understand water dissociation and ion solvation and that the bias-dependent $A(\eta)$ is not caused by surface configurational entropy changes (for the potentials studied), as E_A is constant, but that it probably originates from the interfacial water structure itself.

Bias-dependent capacitance at active sites

With decreasing catalyst loading and activity, we observe that E_A increases at the same potential and further becomes increasingly dependent on the overpotential (for the same loading) (Fig. 2b). We ascribe the increasing E_A with reduced loadings (diagonal lines) to increasing contributions of the low-activity AEL and CEL acid–base sites in the WD catalysis. As in Fig. 2a, changing E_A is compensated by ΔS_{Config}, leading to an increasing total A at 40 mV with decreasing loading (diagonal lines with slopes ≤ 0.1 mol kJ^{-1}). The increasing bias dependence of E_A tends towards an ideal correlation between ΔA and ΔE_A in the limit of no catalyst loading (pristine BPM) over a large potential range (Fig. 2c). In contrast to the electrostatically decoupled oxide catalysts in Fig. 2a, the reaction is now catalysed at the very same polymer sites that are involved into the formation of the electric fields.

At solid–liquid interfaces, the electrochemical bias can manifest itself in two general ways. With constant local chemical potentials, for example a constant protonation state of cation ion exchange groups (CEL−CH), the electrostatic potential drop can energetically irreversibly reduce the activation enthalpy and drive the reaction forward. However, the bias can also lead to energetically reversible charging of interfacial capacitance and changing local chemical potentials, such as when deprotonating (CEL−CH→CEL−C$^-$+H$^+$) and dehydroxylating (AEL−AOH → AEL−A$^+$ + OH$^-$) the very same polymeric ion exchange groups that catalyse the reaction. This energetically reversible charging cannot reduce the activation enthalpy because it does not constitute a thermodynamic driving force. The groups will return to their original state at electrochemical equilibrium. However, reversible charging of interfacial capacitance can still impact the activation entropy of the surface and interfacial water molecules. In Fig. 2c, we observe that the slope with bias (~0.25 mol kJ^{-1}) is substantially larger than any of the slopes assigned to surface configurational entropy changes in Fig. 2a,b (~0.1 mol kJ^{-1}). Thus, we conclude that the emergence of capacitive charge primarily leads to entropic changes in the water network that impact the initial and/or transition state of ion solvation. Because electric fields manifest themselves in both non-equilibrium conditions, we designate the fields linked to energetically reversible charging as capacitive electric fields. As we show below, up to 200 mV, the bias is almost exclusively translated into changes in the interfacial capacitance, which directly correlates with changing pre-exponential factors. Only above 200 mV does the bias slowly reduce the activation enthalpy.

The role of capacitance in entropy−enthalpy relationships

To elucidate the role of bias-dependent interfacial capacitance at different timescales in the enthalpy−entropy relationships of Fig. 2, we performed potential-dependent impedance measurements of the pristine and metal oxide catalysed BPM junction (Methods). For WD potentials up to 1 V, we observe that the impedance is dominated by the junction kinetics across a very large frequency range, from -1 Hz to 500 kHz. This is consistent with the absence of mass transport/diffusion limitations (<1 Hz) (Supplementary Note 1)[37], Faradaic currents (-0.1–100 Hz) stemming from junction limited kinetics (Fig. 1), the large semi-circle in the Nyquist plots and low series resistance (<1 Ω) for all studied BPMs that enables us to extract capacitance up to 500 kHz
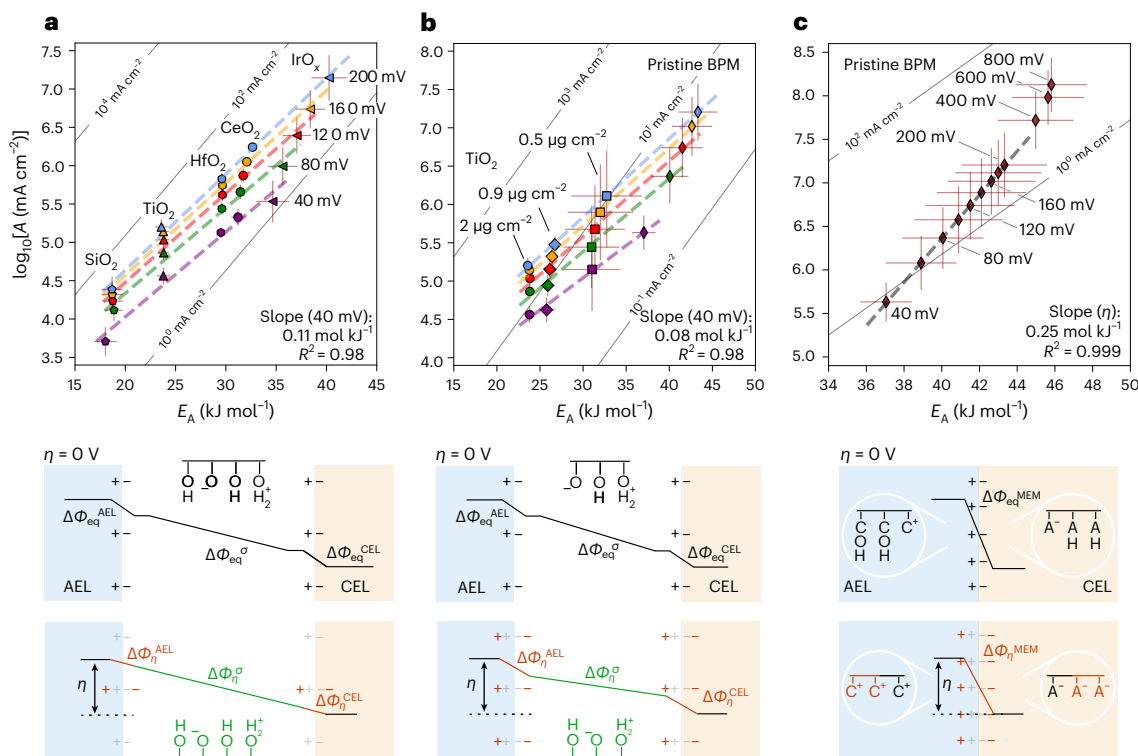
Fig. 2 | Water dissociation and ion solvation for varying degrees of capacitive coupling. a, Across metal oxides at the same bias, we observe compensation between the activation energy and pre-exponential factor. Under bias, the acid–base chemistry of the metal oxide catalyst is unchanged (E_A constant) and electrostatically decoupled from the electrostatic potential drop, $\Delta\Phi$, ($\Delta\Phi_\eta^\sigma + \Delta\Phi_\eta^{AEL} + \Delta\Phi_\eta^{CEL}$) across the junction ($\sigma$). Whereas $\Delta\Phi_\eta^{AEL}$ and $\Delta\Phi_\eta^{CEL}$ are implied in establishing the (capacitive) electric fields across the junction, the kinetics (E_A and A) primarily stem from WD driven at the active metal oxides in the presence of $\Delta\Phi_\eta^\sigma$. The electric fields alter the activation entropy during (de) solvation. Loadings are 15 µg cm^{-2}, except 2 µg cm^{-2} for TiO$_2$ (more loadings in Supplementary Fig. 6). **b**, With decreasing TiO$_2$ catalyst loading and junction activity, the membrane's acid–base groups increasingly contribute to the junction kinetics. In these membrane space charge regions, the bias increasingly changes the local chemical potentials, μ, ($\Delta\mu_{eq} \neq \Delta\mu_\eta$) between equilibrium (eq) and applied bias (η) by deprotonating (dehydroxylating) fixed anionic (cationic)

groups. **c**, Without additional metal oxide catalyst (pristine BPM), water dissociation is now exclusively driven on the acid–base sites with bias-dependent coverage $\eta \approx \Delta\Phi_\eta^{MEM}$ (red), resulting in bias-dependent $E_A(\eta)$ and $A(\eta)$. Up to 200 mV, the bias is fully translated into energetically reversible capacitance, that is $\eta = \Delta\Phi_\eta^{AEL} + \Delta\Phi_\eta^{CEL} = \Delta\Phi_\eta^{MEM}$ where $\Delta\Phi_\eta^{MEM}$ is the total electrostatic potential drop across the polymeric junction. The diagonal lines show simulated current densities at 65 °C. Shown values are means, and error bars show standard deviation for E_A (slope) and A (intercept) from Arrhenius analysis, based on five observations (temperatures). The black lines designate the electrostatic potential drop at electrochemical equilibrium, the green lines the potential drop across the metal oxide catalyst sites at applied bias and the red line the electrostatic potential drops at the interface of the AEL and CEL at applied bias. The black and grey (red) plus and minus signs represent the membrane space charge at equilibrium (applied bias).

(Supplementary Figs. 7 and 8). We extract the real part of the capacitance, $C_R(\omega)$, according to $C_R(\omega) = -Z(\omega)_I(\omega |Z(\omega)|^2)^{-1}$ (Supplementary Fig. 9) with the frequency (ω) dependent imaginary impedance, $Z(\omega)_I$, and the absolute value of the impedance, $|Z(\omega)|$, as we can associate it with the reversible amount of energy stored at the interface, whereas the imaginary part is related to (more complicated) dissipative processes for a simple RC (resistor–capacitor) circuit[38,39]. Here we refrain from fitting the data with traditional equivalent circuits, where the Faradaic current is only dependent on the charge transfer resistance and not promoted by the build-up of capacitive charge.

When we correlate $C_R(\nu,\eta)$ with $\log_{10}A(\eta)$ and $E_A(\eta)$, we discover strong correlations ($R^2 \approx 0.98–1$) for the pristine and also oxide BPMs (Supplementary Figs. 10–12). For E_A near equilibrium ($\eta = 40$ mV), we find that E_A correlates logarithmically with the capacitance at the high-frequency inflection point of the phase angle around 5–10 kHz and more linearly at the maximum of the phase angle up to 100 kHz (Fig. 3a). This result supports our hypothesis that E_A is primarily determined by the oxide's point of zero charge and local pH at the membrane's interface at equilibrium. Similarly, for the pristine BPM and polymeric acid–base groups, this high-frequency capacitance is linked to the deprotonated/dehydroxylated groups in the space charge regions. Together with Fig. 2a, the results demonstrate that ΔS_{config} is

also linked the reversible amount of energy stored at high frequencies, bridging catalysis and energy storage science[40]. For $\Delta A(\eta)$ we find a close correlation with $\Delta C_R(\nu,\eta)$ at 1–100 Hz (Fig. 3b), that is, at frequencies where Faradaic processes (due to $\Delta A(\eta)$) are dominating the impedance. Finally, when combining the capacitances for $E_A(\eta)$ and $A(\eta)$ for the oxides, we are able to retrieve the trends in Fig. 2a, that is, the high-frequency capacitance remains constant, as does $E_A(\eta)$ (Fig. 3c). In contrast, for the pristine BPM, the high-frequency capacitance changes with bias, consistent with our assignment of bias-dependent space charge capacitance (Fig. 3d). Similar to Fig. 3c, we also find a close correlation ($R^2 \approx 0.99$) for the pristine BPM directly between $|\Delta C_R(\nu,\eta)|$ at 300 kHz and capacitive components emerging at Faradaic currents at 1 Hz (Supplementary Fig. 13). Taken together, our results demonstrate that the activation energy (activation enthalpy) and pre-exponential factor (activation entropy) in the Arrhenius rate law are directly linked to a bias-dependent interfacial capacitance.

The build-up of capacitive charge on the solid (polymer) side is balanced by capacitive processes on the electrolyte side, such as water reorientation or ion accumulation. While it is difficult to separate these, we do observe maxima in the imaginary impedance, $Z_I(\nu)$, that can be used to identify the time constants of individual processes ($\tau_i = (2\pi\nu)^{-1}$) (Supplementary Figs. 15 and 16). For WD potentials,
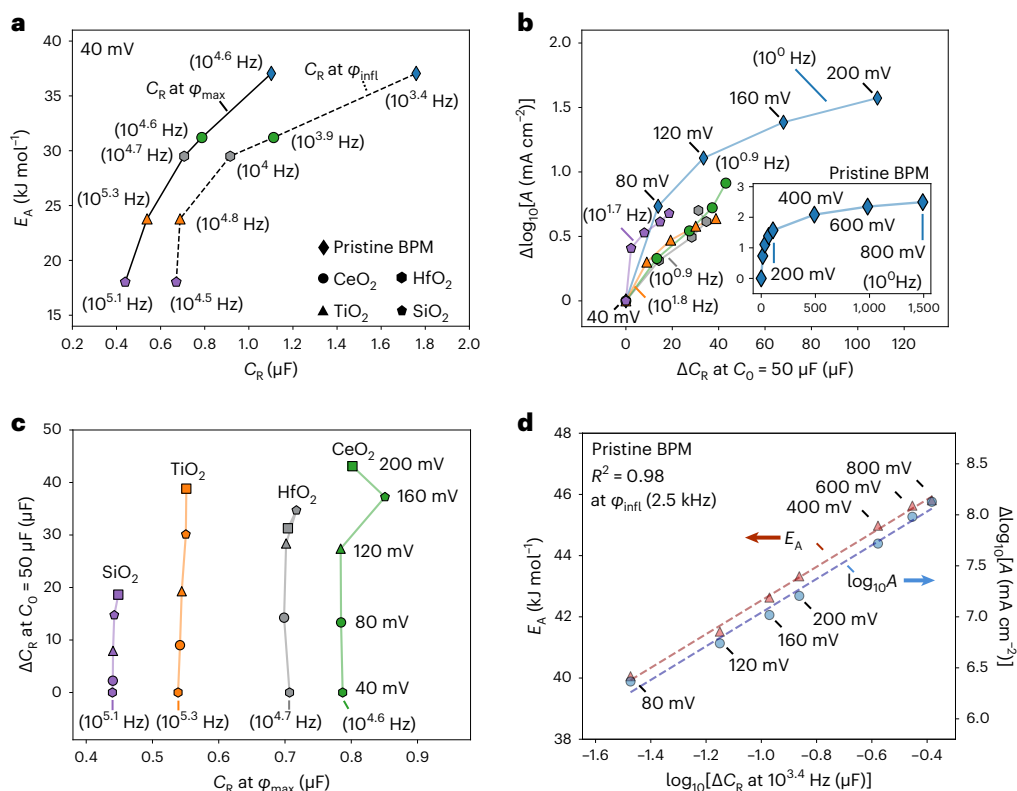
Fig. 3 | The role of interfacial capacitance in bias-dependent entropy–enthalpy relationships. a, E_A near equilibrium ($\eta = 40$ mV) depends logarithmically on the C_R at the inflection point, φ_{in}, or more linearly at the maximum, φ_{max}, of the phase angle for each BPM, corresponding to C_R at 1–100 kHz. **b**, $\Delta\log_{10}A(\eta)$ correlates logarithmically with the change ΔC_R starting from $C_R(\nu, 40$ mV$) = 50$ μF for each BPM, corresponding to capacitance related to Faradaic currents at 1–100 Hz. See legend in **a** for symbol assignment. Inset: the $\Delta\log_{10}A(\eta)$ versus ΔC_R correlation up to 800 mV for the pristine BPM.

The x- and y-axis labels and units from the main graph also apply to the inset. **c**, When we correlate C_R at the maximum phase angle, φ_{max}, at 10–100 kHz (**a**) with ΔC_R at 1–100 Hz (**b**), we retrieve qualitatively a very similar trend to Fig. 2a (C_R at inflection point in Supplementary Fig. 14). **d**, For the pristine BPM, we find a linear correlation ($R^2 \approx 0.99$) between $|\Delta C_R|$ at 2.5 kHz with E_A and $\Delta\log_{10}A(\eta)$, consistent with the trend in Fig. 2c. Importantly, an increase in $|\Delta C_R|$ reflects a decrease of C_R at 100 kHz (Supplementary Fig. 10 for ΔC_R), indicating a frequency dispersion of interfacial capacitance.

we observe peaks that we can directly associate with the processes discussed above. Strikingly, for WF potentials, a peak emerges at $\tau_2 \approx 10^{-4}$ s, just above the characteristic timescale of ice structures in water ($\sim 10^{-3}$ s) (Supplementary Note 3 and Supplementary Fig. 16). Whereas operando solvent spectroscopy[14] will be needed to determine the exact origin, our results indicate that double layer relaxation timescales are substantially slowed down compared with bulk water, consistent with molecular dynamics (MD) on ordered interfacial water[2,6].

Our observations of bias-dependent pre-exponential factors, the emergence and absence of entropy–enthalpy compensation and the link to a (bias-dependent) frequency dispersion of capacitance have never been shown that comprehensively before in electro-, bio- or thermal catalysis, let alone BPM science. Nonetheless, individual aspects of it have been reported before in electrocatalysis. At metal–electrolyte interfaces, instead of deprotonation and dehydroxylation at (electronically non-conducting) polymer groups, capacitive charge can emerge due to electronic polarization, ion accumulation, incomplete phase transitions and charged intermediates. For example, Bockris et al. linked frequency-dependent double layer resistance and capacitance to bias-dependent interfacial water relaxation times (in the non-Faradaic region) but could not link it to activation entropy changes[41]. Later, Conway et al. observed bias-dependent pre-exponential factors for H_2 evolution on Hg and Br_2 evolution on vitreous carbon and concluded that non-equilibrium electric fields might change the activation entropy[42,43]. Schmickler and coworkers have performed seminal MD simulations on the influence of capacitive charge on interfacial H_3O^+ (de)solvation during the HER in acid on high

overpotential metals[2]. By calculating the free energy of (re)orienting a (shuttle) water molecule in the first adsorbed water layer, the MD simulations qualitatively predicted increasing activation energies with increasing capacitive charge. As the simulations were limited to biases near the potential of zero charge, they could not inform on entropic changes of the pre-exponential factor or compensating enthalpic changes. The authors also discussed the possibility of an increasing reactant (H_3O^+) concentration and reduced distance to the electrode surface that could lead to an effective increase in the pre-exponential factor with applied bias for the HER in acid. However, for WD inside the BPM, the H_2O concentration is very high and essentially constant on the hydrophilic metal oxide surfaces for the current densities studied. Below, we will show that ion solvation in BPMs is governed by the same physics as ion solvation in electrocatalysis.

A semi-empirical multiphysics solvation model

Our results enable us to develop a multiphysics model based on regular Nernst–Planck transport and first-order electrochemical Arrhenius rate laws for forward WF and reverse WD rates according to a general electrochemical kinetics formalism:

$$j_{total} = k_{WD} - [H^+][OH^-]k_{WF} \qquad (3)$$

where k_{WD} and k_{WF} follow equation (1). In contrast to previous bipolar membrane-specific or electrocatalytic (Butler–Volmer-type) models, we do not assume constant pre-exponential factors but instead extract $A(\eta)$ and $E_A(\eta)$ from experiments. Thus, we avoid artificial restrictions
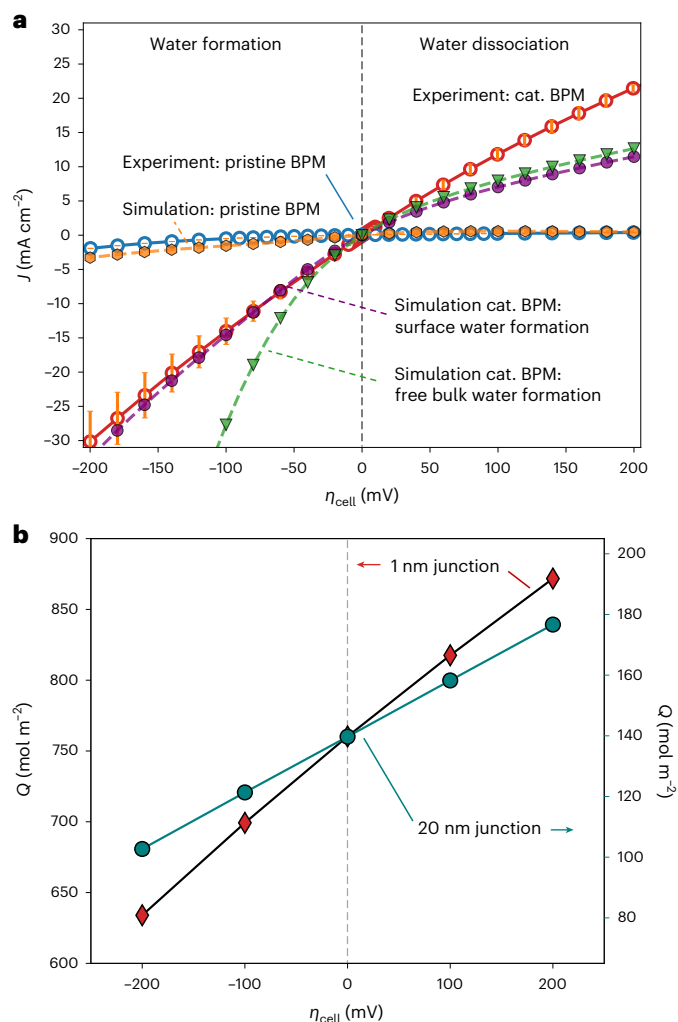
Fig. 4 | Multiphysics model and experimental polarization curves. The model is based on regular Nernst–Planck equations and Arrhenius rate laws for the WD and WF rates in the junction ($r_{total} = r_{WF} + r_{WD}$) and uses experimentally determined A and E_A. **a**, Simulated and experimental polarization curves for a pristine BPM (orange and blue) and for a BPM with added metal oxide catalyst (cat. BPM) for WF and WD currents at 25 °C (green, purple and red). For WF currents, we have to include Langmuir adsorption on the metal oxides (purple) for [H$^+$] and [OH$^-$], otherwise the WF currents increase too quickly (green). For the low currents shown, [H$_2$O] is constant in the hydrated polymers. **b**, Simulated bias dependence of space charge for pristine BPM (1 nm junction, 0.6 mol m^{-2} mV^{-1}, red) and with metal oxide (20 nm junction, 0.2 mol m^{-2} mV^{-1} turquoise).

imposed by the absence of temperature-dependent kinetic datasets and oversimplified theory. Currently, the exact analytic form of $A(\eta)$ is unknown. As the experiments only inform on the total A, we cannot extract the individual As for WD and WF separately. However, by comparing our results across bipolar and electrocatalytic junction and literature data, we retrieve an approximate form for $\Delta \log A \approx a \times \log_{10}(\eta) + b$ (more below; Methods, Supplementary Note 4, Supplementary Tables 1 and 2 and Supplementary Figs. 17–19).

Our simulated and experimental kinetics give satisfying agreement (Fig. 4a). Qualitatively, we do not observe any changes when varying experimentally unknown parameters, such as the exact junction thickness, which validates our approach. Our model demonstrates that regular Nernst–Planck transport and electric field strengths can give rise to BPM behaviour as long as the pre-exponential factor is left bias dependent. This a substantial advance over previous BPM models that postulate more complicated physics and introduce many additional

tuning parameters (Supplementary Table 1). Our simulations also confirm that thin low-activity junctions comprise more space charge than thicker junctions with high activity oxides (Fig. 4b), whereas the exact amount depends on quantities unknown, such as the exact local dielectric constants in the polymer layers. To simulate WF currents, we have to include Langmuir adsorption on the metal oxide surface (purple) instead of free OH$^-$ and H$^+$ recombination (green), in line with a full catalytic picture of the BPM junction.

From polymer–polymer to electrolyte–metal interfaces

Capacitive charge not only emerges at polymer–polymer (Fig. 5a) but also electrolyte–metal interfaces (Fig. 5b,c). Here to elucidate the ion (de)solvation kinetics at electrolyte–metal interfaces, we studied a bipolar junction between liquid KOH and a PdAg-H membrane (Fig. 5b). Recently, it has been shown that the overpotential of the charge transfer step of the alkaline HER (involving WD and hydroxide solvation) can be studied in isolation at a liquid electrolyte–PdH membrane[44], which is placed in an H-cell between two compartments and characterized via a four-point measurement. Here we form a bipolar junction and study the kinetics of H$_2$O + M* + e$_M^-$ → HM + OH$^-$, that is, interfacial water dissociation and OH$^-$ solvation in isolation at a metallic PdAg foil (Supplementary Fig. 20). Compared with Pd, PdAg (75:25) shows better stability against hydrogen embrittlement. We further study the HER kinetics on the same PdAg foil, which includes the charge transfer step and the chemical Tafel step. At the current densities studied, we do not observe any impact of the fast Tafel step, consistent with the results by Tang et al.[44].

For WD and OH$^-$ solvation at the 0.1 M KOH–PdAgH interface, we find the same slope $\Delta \log(A) \times \Delta E_A^{-1} \approx 0.25$ mol kJ^{-1} (blue line in Fig. 5d), as for the pristine BPM (orange line). Further, when we study HER kinetics on the same PdAg, we obtain essentially the same slope of -0.24 mol kJ^{-1} (purple line). As H$^+$ solvation is absent for the KOH|PdAg interface (H$_2$O + M* + e$_M^-$ → HM + OH$^-$) but present during BPM WD (H$_2$O ↔ H$^+$ + OH$^-$), this implies that BPM kinetics are primarily governed by water dissociation and OH$^-$ solvation kinetics. The same slope across dissimilar interfaces further indicates that there exists a *solid structure-independent* bias dependence of A and E_A. Despite the different acid–base chemistry and different origin of capacitive charge for polymer and metal interfaces, the structure-independent slopes support our hypothesis that the bias-dependent $A(\eta)$ is caused by (capacitive) electric fields that change the entropy of interfacial water at the initial or transition state of ion solvation. Figure 5e shows literature data for the HER on polycrystalline Au and Ag (111) in 1 M HClO$_3$ with slopes of 0.31 mol kJ^{-1} and 0.42 mol kJ^{-1}, respectively. This is consistent with faster H$^+$ than OH$^-$ (de)solvation and a different influence of electrolyte ions on the capacitance and HER kinetics for different metals[3,4,45,46]. Figure 5f–g shows $A(\eta)$ across interfaces and qualitatively match Fig. 3b. Whereas the electric field will vary between polymeric space charge regions (~1–5 nm) and sharper electrolyte–metal interfaces (0.3–1 nm), the trends are very similar with $\Delta \log A \approx a \times \log_{10}(\eta) + b$ up to -200 mV.

Conclusions

Our results help draw a new picture of electrocatalysis and electrochemistry in general[2]. Butler–Volmer theory, which originated from outer-sphere electrochemistry and thus reactions that do not involve interfacial ion (de)solvation, focuses on the reduction of the activation free enthalpy by the electron electrochemical potential. This approach is incorrect in the generality it is currently applied and taught for inner-sphere electrochemistry, where the pre-exponential factor can be bias dependent. Even close equilibrium, the activation enthalpy and (configurational) entropy are coupled and can lead to (apparent) compensation, as shown here for metal oxides and previously reported for HER electrocatalysts close to electrochemical equilibrium[47,48].
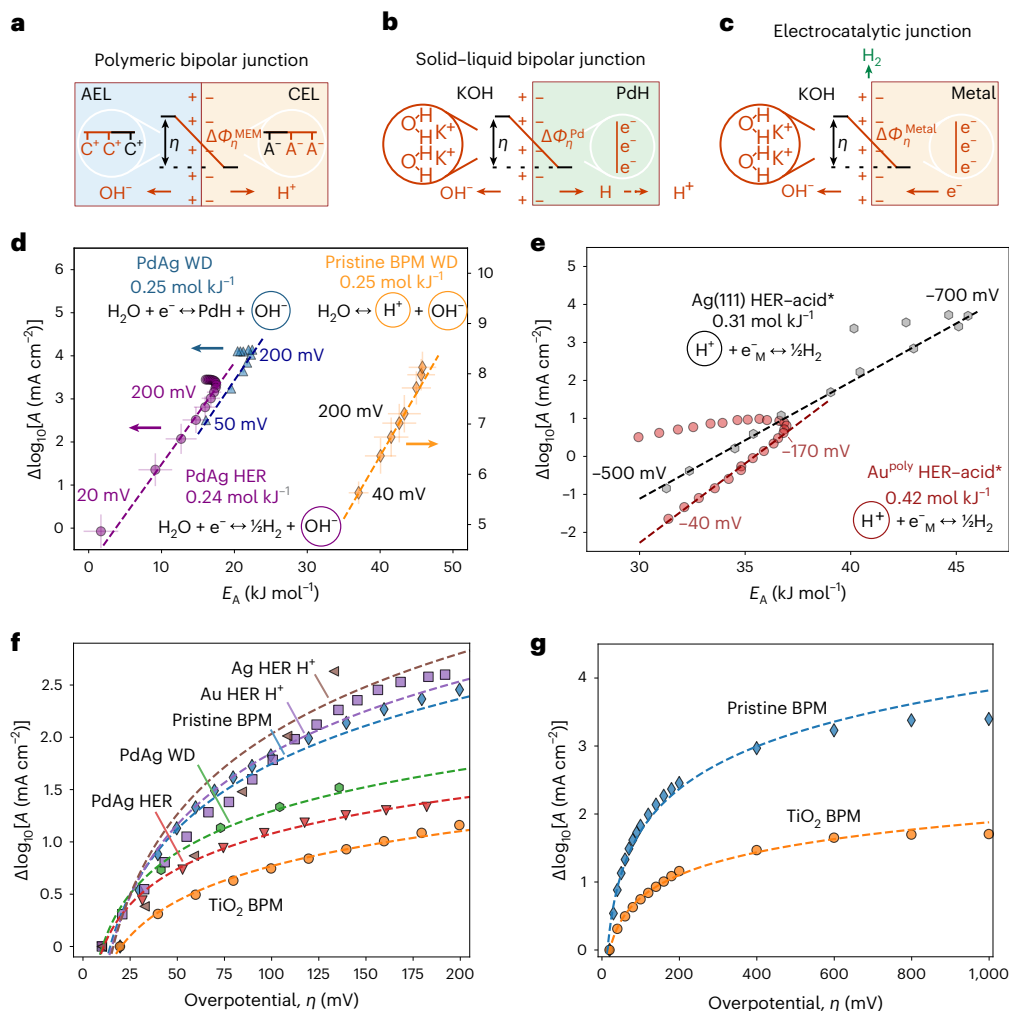
Fig. 5 | Entropy–enthalpy relationships during ion (de)solvation at capacitive interfaces. The same physical principles govern interfacial (de)solvation in BPMs and at electrocatalyst interfaces. **a**, In the pristine BPM, catalysis occurs at acid–base sites in the membrane space charge regions that change their protonation/hydroxylation state upon polarization. **b,c**, At liquid–PdH (**b**) and liquid–electrocatalyst (**c**) interfaces, capacitive charge can emerge for example due to electronic polarization, ion accumulation and incomplete phase transitions. The shaded areas designate the AEL (blue), CEL (yellow), PdH foil (green) and a metal foil without hydride formation (yellow). For meaning of the red symbols see caption of Fig. 2. The red color shows the processes under bias. **d**, Strikingly, the WD activities of pristine BPMs (involving H^+ and OH^- solvation), metal–liquid bipolar junctions (involving OH^- solvation) and alkaline HER

(involving OH^- solvation) display an almost identical slope for potentials up to $0.2\,V_{RHE}$, indicating that BPM kinetics are strongly influenced by OH^- solvation and a structure-independent relationship between dA and dE_A. RHE, reversible hydrogen electrode. **e**, Literature data, indicated by asterisks, of $d\ln A/dE_A$ for acid HER on Ag(111) and Au^{poly} involving interfacial H^+ desolvation[59,60]. **f**, Our and literature data[59,60] and heuristic model $A_{cap} \approx a \times \log_{10}(\eta) + b$ showing the similarities between ion (de)solvation in BPMs and electrocatalysis. **g**, The BPMs show sub-logarithmic trends at higher bias, either due to saturation of H_2O ordering or limitations of forming electric fields via polymer space charge regions. Data for Au and Ag HER from refs. [59,60]. Values are means, and error bars show standard deviation for E_A (slope) and A (intercept) from Arrhenius analysis, based on five observations (temperatures) for BPMs and PdAg HER.

Accounting for a bias-dependent activation entropy and enthalpy may enable new electrochemical energy technology. For example, tuning the solvation kinetics selectively for desired ions could enable improved membrane ion selectivity, catalyst activity, product selectivity and corrosion resistance. Similarly, ion solvation kinetics are probably pivotal when interfacing electrochemistry with thermochemical reactions to exploit strong electric fields for large rate enhancements[49].

Beyond electrochemistry, our results might be important for the working principle of ion motors and ion pumps[50,51]. Directional proton transport across the rotary motor of adenosine triphosphate synthase must entail proton (de)solvation, which, according to our results, will lead to the emergence and possibly displacement of capacitive charge that could trigger conformational (rotational) changes, for example, against a fixed stator charge[52–54]. Along similar reasoning, interfacial capacitive excess charge is probably fundamentally implied in conformational enzyme dynamics and kinetics and will provide a more

comprehensive descriptor than bulk rate constants alone[55]. Stark spectroscopy studies have highlighted the importance of strong electric fields in biocatalysis[56,57]. Here we show that electric fields linked to interfacial capacitance are impacting the activation entropy during ion (de)solvation. In general, tuning the activation entropy can maximize energy conversion efficiency—something that evolution must have exploited right from the start and something we have to catch up to for a new generation of electrochemical processes with profoundly greater activity, selectivity and stability.

Methods
Membrane and ionomers
Nafion 212 (Fuel Cell Store) was used as the cation exchange layer (CEL). The as-received membranes were cut into $4 \times 4\,cm^2$ pieces and immersed for at least 24 h in deionized water before further use. PiperION-A25-HCO3 (Versogen) was used as anion exchange layer

(AEL). The as-received membranes were cut into 1.5×1.5 cm^2 pieces and immersed in 0.5 M KOH for at least 2 h after which the KOH was renewed, leaving the pieces in the solution for at least another 24 hours. Nafion 520 (Sigma Aldrich) was used as an ionomer to prepare the electrodes in the membrane electrode assembly facing the CEL, whereas a dispersion of PiperION-A25-HCO3 in ethanol (Versogen) was used as the ionomer for the electrodes facing the AEL.

Electrode preparation

The gas diffusion electrodes (GDEs) were fabricated by spray coating a dispersion containing the Pt/C electrocatalyst and respective ionomers onto Freudenberg H23C2 (Fuel Cell Store). Two sets of GDEs were prepared, one with Nafion to face the CEL and another with PiperION to face the AEL. The dispersions were prepared by mixing 100 mg of Pt/C 70% (Thermo Fisher Scientific) and 400 mg of the ionomer solution with 0.5 g of H_2O and 1.7 g of isopropyl alcohol (IPA). The electrodes had a dry ionomer loading of 20%wt The dispersions were sonicated for at least 4 h before spraying each onto Freudenberg H23C2 cut to ~5 × 5 cm^2 and heated at 85 °C. The resulting total loading ranged between 1.5–2 mg cm^{-2}.

Metal oxide nanoparticle spray coating

Commercial P25-TiO$_2$ (20 nm, Sigma Aldrich), SiO$_2$ (20 nm, Nanocomposix), IrO$_x$ (3 nm Fuel Cell Store), CeO$_2$ (10 nm, US-Nano) HfO$_2$ (60–80 nm US-Nano) were deposited inside the BPM junction at low loadings ≤15 µg cm^{-2} to minimize the impact of extended surface oxide transport. To that end, the particles were dispersed in 0.5 g of H_2O and 1.7 g of IPA and sonicated for at least 4 h (longer times of up to 12 h were used for IrO$_2$ dispersions). Then the particles were spray coated onto Nafion 212 taped on a preheated glass substrate at 85 °C. The corresponding membrane loading (L) was calculated using the formula:

$$L = \frac{w_0 \times R_c}{A_m} \tag{4}$$

where w_0 is the mass of the nanoparticles used to prepare the dispersion, A_m is the spray-coated area of the membrane (generally 4 × 4 cm^2) and R_c is a retaining coefficient close to 25%, estimated from repeated spray coating on a SiO$_2$ wafer with TiO$_2$-P25 and subsequent weighing (Supplementary Table 3).

Membrane electrode assembly

To perform the electrochemical measurements of the BPM assembly, the membranes and electrodes were integrated into a regular membrane electrode assembly (MEA) in a fuel cell set-up (Supplementary Fig. 1). First, a Pt/C-PiperION GDE is placed inside the gasketing space. Next an ion exchanged and thoroughly washed (twice in ultrapure water) PiperION-A25 (25 µm) membrane is placed with care on top of the GDE making sure that the electrode is fully covered. Afterwards, a Nafion 212 membrane (50 µm) is placed on top of the PiperION membrane forming the Bipolar Membrane (BPM) assembly. The hydrated Nafion membrane may be as received (already ion exchanged) forming a 'pristine' BPM or spray coated on one side with the metal oxide nanoparticle catalysts. Finally, another 250 µm gasket is placed on top of the Nafion and a PtC-Nafion GDE is placed on top followed by another graphite block, current collector and stainless-steel support. The whole stack is fixed with eight screws with a torque wrench at 6 Nm. MEAs are used in anion exchange membrane (AEM) and proton exchange membrane (PEM) electrolysers and fuel cells. They provide continuous physical compression among all layers during operation. The zero-gap contact between GDEs and ionically conductive membranes allows us to operate the stack in the absence of any liquid electrolyte, feeding only gases that are humidified with pure water.

Electrochemical set-up and initial stabilization

The electrochemical experiments were performed using a Gamry® Reference 3000 potentiostat with a fuel cell humidification system (Fuel Cell Technologies Inc, Model LFHS-C) that controls the cell temperature and gas temperature, humidification, flow rate and pressure. H_2 is fed to the anode and cathode, that is, the cell is operated as a H_2 pump. Due to the fast kinetics of the 2 mg cm^{-2} HER/HOR PtC GDEs and the two orders of magnitude dissimilar catalyst loadings to the ultra-low loading (≤ 20 µg cm^{-2}) junction, the total cell potential informs directly on the junction kinetics in the potential range studied (Supplementary Fig. 2). For water formation (WF), HOR is driven at the acidic Nafion GDE (generating protons), whereas the HER is driven at the alkaline PiperION GDE (generating hydroxides). As a result, protons and hydroxides are injected into the junction and form water. For water dissociation (WD), the HER is driven on the acidic electrode (consuming protons), whereas the HOR is driven at the basic electrode (consuming hydroxides) (Supplementary Fig. 1). As a result, the water is forced to dissociate inside the junction. For initial stabilization, humidified H_2 gas heated to 65 °C was fed into the MEA cell through heated inlets at 70 °C (preventing condensation) until a back pressure of 1 bar was obtained for both electrode chambers. Then, the cell was heated from room temperature to 63 °C. During this process, a chronoamperometric measurement at 200 mV WF potentials was performed to track the evolution of the current for the duration of the heating process (~45 min). This initial measurement tracks the stabilization process where the electrodes are slowly being freed of an oversupply of water during the heating process. Once the system is stabilized, a bias of −1,000 mV (WD) was applied for a short time (2–5 min) followed by another potential step for 5 min at 200 mV (WF), as we found that this stabilization protocol improved the reproducibility and stability of the measurements. Note that the sign of the applied experimental potential was swapped when analysing the data to assign positive currents and potentials to WD and negative ones to WF.

Symmetric $I–V$ curves for metal oxide catalysts imply the absence of potential-dependent dynamics of the electrically isolated metal oxide nanoparticles. During WD, mobile ions besides H^+ and OH^- are unlikely present, as the cell is operated with pure H_2O humified gases and continuously flushes positive and negative (trace) ions outward from the junction. For WF potentials, trace ions might accumulate.

BPM temperature measurements

Starting with the equilibrated cell at 63 °C, chronoamperometry from WD to WF potentials was performed (the reverse for the pristine BPM). Each potential was held between 1–3 min, depending on the potential and current range, to ensure a stable steady-state performance (Supplementary Fig. 3). Then the measurements were repeated for different temperatures of the cell, gas and inlets. The cell temperatures were 63, 53, 43, 33 and 23 °C, the H_2 gas temperatures 65, 55, 45, 35 and 25 °C and the heated (anti-condensation) inlets 70, 60, 50, 40, 30 °C, respectively. The temperature of the MEA cell was kept 2 °C below the one of the humidified H_2 to ensure sufficient hydration of the GDEs while also preventing flooding.

Impedance measurements

Starting from the equilibrated cell at 63 °C, three impedance measurements of varying amplitude were performed (± 10 mV, ± 5 mV, ± 1 mV) after each (1–3 min) stabilized potential between 0.1 Hz and 1,000 kHz. We started with WD biases (−200, −160, −120, −80, −40 mV), followed by equilibrium at 0 mV and finally continued to WF biases at 40 mV, 80 mV, 120 mV, 160 mV and 200 mV.

Metal foil measurements

The PdAg (75:25) foils (Fisher Scientific) were cleaned in 1:2 H_2O_2:HNO$_3$ for 15 min, followed by a thorough pure water rinse. Then the foils were

mounted into a custom plastic (HDPE)) H cell with electronic leads made from titanium. A leak-less Ag/AgCl (eDAQ) reference electrode was used, together with a Pt counter electrode (separated with a Pipe-rion membrane) in the analytic chamber, whereas another Pt counter electrode was used in the auxiliary compartment. The analytic cham-ber (with the reference electrode) was filled with 0.1 M KOH (Fisher Scientific, semiconductor grade) and sparged with Ar to remove O_2. The auxiliary chamber was filled with 0.1 M H_2SO_4 (99.99%). The foil area was taken as the one defined by the two o rings separating the compartments. Before WD measurements, the metal membrane was charged for 10 min at 200 mA cm^{-2} between the two counter electrodes. Afterwards, bubbles were removed from the foil surface with a plastic pipette. For the WD measurements, current was driven between the two counter electrodes and the potential of the PdAg membrane was measured vs the Ag/AgCl electrode. By subtracting the equilibrium open-circuit potential from the measured potential, the overpoten-tial for the interfacial WD reaction (involving OH$^-$ solvation) can be extracted. For more details the reader is referred to the recent publica-tion by Tang et al.[44]. For the temperature-dependent measurements. The whole H cell was placed into a separately heated temperature bath. To determine the WD overpotential directly, chronopotentiometry was performed as shown in Supplementary Fig. 20 as we observed a small shift of the open-circuit potential, which prevented us from performing comparative chronoamperometry measurements. For HER measurements, regular chronoamperometry was performed (Supplementary Fig. 20).

COMSOL multiphysics simulations

COMSOL Multiphysics 6.0 was used to perform the Finite Element Method to solve partial differential equations that describe WD and WF according to our interfacial solvation model (Supplementary Note 4), the electrostatic profiles and the H$^+$ and OH$^-$ transport. No additional electrolyte was introduced, consistent with our experiments. The Ter-tiary Current Distribution Module was used to describe the BPM-MEA in three domains, a CEL, the BPM junction and the AEL. Applying the Finite Element Method, these domains were discretized in small domains where the governing equations are solved. First, the mass conservation equation is solved for the i species (H$^+$, OH$^-$):

$$\frac{\mathrm{d}N_i}{\mathrm{d}x} = R_i \tag{5}$$

This assumes that sources/wells in the molar flux of the species are caused by chemical reactions at that point of the grid, according to R_i, which is the volumetric generation/consumption of species. For the extended AEL and CEL domains, R_i is described by water auto-dissociation equilibrium:

$$R_{H_2O} = k_f - k_r c_{H^+} c_{OH^-} \tag{6}$$

where c is the concentration of each species. For the BPM junction, our ion solvation model is used to account for the metal oxide and mem-brane acid–base site WD and WF catalysis (above). The molar flux of species N_i is described by regular Nernst–Planck–Poisson equations, where the gradient of the electrochemical potential ($\bar{\mu}_i$) is the driving force for the transport:

$$N_i = -\frac{c_i D_i}{RT} \nabla \bar{\mu}_i \tag{7}$$

where D_i and c_i are the diffusion coefficients and the concentration of each species, respectively. This equation can be expanded mathe-matically into two terms. A first one that describes the chemical part, where the gradient of the concentration drives the transport (equiva-lent to Fick diffusion) and a second term which accounts for the migra-tion of charged species in the presence of an electrostatic potential gradient (ϕ):

$$N_i = -D_i \nabla c_i - \frac{c_i D_i z_i F}{RT} \nabla \phi \tag{8}$$

where z_i is the charge number of each species. The conservation of charge in the model is established by solving Poisson's equation:

$$\nabla^2 \phi = \frac{F}{\varepsilon \varepsilon_0} \left(c_M + \sum_i z_i c_i \right) \tag{9}$$

where ε_0 is the permittivity of vacuum, ε is the permittivity of the mod-elled domain and c_M is the fixed charge density of the membranes. Through c_M, membrane charge selectivity is introduced in the simula-tion. The spatial description of c_M is done with hyperbolic tangents to account for a smooth variation between domains, as introduced by Bui et al. (for a second Wien-effect model)[58]:

$$c_{CEM} = \frac{CEM_{Cfix}}{2} \tanh\left(\frac{x + CEM_{limit}}{L_{char}}\right) + \frac{CEM_{fix}}{2} \tag{10}$$

$$c_{AEM} = \frac{AEM_{Cfix}}{2} \tanh\left(\frac{x + AEM_{limit}}{L_{char}}\right) + \frac{AEM_{fix}}{2} \tag{11}$$

$$c_M = c_{AEM} + c_{CEM} \tag{12}$$

where AEM_{fix} and CEM_{fix} are the nominal charge densities of the membranes, calculated from the product of the ion exchange capacity of the membrane and its wet density, AEM_{limit} and CEM_{limit} are the coor-dinates of the interface between the junction and membrane domains with respect to the junction centre, x is the spatial coordinate of the 1D simulation and L_{char} is a parameter that sets the slope of the tanh variation.

Hyperbolic tangents are useful to describe a smooth variation of a parameter across the interface between different simulation domains[58]. Thus, we also employ them for the spatial variation of the dielectric permittivity, too:

$$\varepsilon = \varepsilon_M + \left(\frac{\varepsilon_j - \varepsilon_M}{2}\right)\left[-\tanh\left(\frac{x + AEM_{limit}}{L_{char}}\right) + \tanh\left(\frac{x + CEM_{limit}}{L_{char}}\right)\right] \tag{13}$$

where ε_M is the dielectric permittivity in the membrane domains and ε_j the permittivity in the BPM junction. This dielectric profile assumes the same value for both AEL and CEL. The diffusion coefficients of H$^+$ and OH$^-$ across the simulation domains are treated in the same manner:

$$D_i = D_i^M + \left(\frac{D_i^j - D_i^M}{2}\right)\left[-\tanh\left(\frac{x + AEM_{limit}}{L_{char}}\right) + \tanh\left(\frac{x + CEM_{limit}}{L_{char}}\right)\right] \tag{14}$$

Where D_i^M is the diffusion coefficient of the i species in the membrane domains and D_i^j the diffusion coefficient of the species in the BPM junction.

For the outer boundaries of the simulation Dirichlet boundary conditions were chosen, imposing fixed concentrations in the limits of the CEL (1,000 mol m^{-3} H$^+$, 10^{-11} mol m^{-3} of OH$^-$) and AEL (1,000 mol m^{-3} OH$^-$, 10^{-11} mol m^{-3} of H$^+$) outer boundaries. The electrostatic potential at the CEL boundary was set to 0 V and the one of the AEL was set to the experimentally applied overpotential, considering the equilibrium potential characteristic from a BPM junction (Supplementary Note 4). The simulation mesh consisted of a total of 6,276 elements. For the BPM junction, a total of 1,500 elements were used with element ratio of 500 distributed in an exponentially towards the AEL and the CEL interface. For the AEL and CEL domains, a size distribution was chosen

with a maximum element size of 10^{-6} m, a maximum growth rate of 500 and 1,250 elements used for the resolution of narrow regions (towards the BPM junction interface and the outer boundaries of the simulation). The direct solver was MUMMPS with a relative tolerance of 10^{-6}, 150 maximum number of iterations and a minimum damping factor of 10^{-40} for the automatic (Newton) nonlinear method. The simulation consisted of three steps. An initial optimization of the equilibrium state at 830 mV (equilibrium potential of a BPM with 1 M membranes; Supplementary Note 4), a first swipe towards 200 mV in the WD direction and a final swipe from 200 mV to −200 mV covering the complete simulated range in a single swipe for easier collection of the data. The swipe direction does not affect the results. All the parameters chosen for the calculations are collected in Supplementary Table 2. Unless stated otherwise, these are the values used for the calculations shown.

Data availability
All data supporting the findings of this article are available in the paper and in the Supplementary Information. Additional data are available from the corresponding author upon reasonable request. Additionally, source data for Figs. 1–5 are provided with this paper. Source data are provided with this paper.

Code availability
The multiphysics code developed for the simulations in this project is described in detail in the Supplementary Information and made available from the corresponding author upon reasonable request.

References
1. Santos, E., Quaino, P. & Schmickler, W. Theory of electrocatalysis: hydrogen evolution and more. *Phys. Chem. Chem. Phys.* **14**, 11224–11233 (2012).
2. Pecina, O. & Schmickler, W. A model for electrochemical proton-transfer reactions. *Chem. Phys.* **228**, 265–277 (1998).
3. Ojha, K., Arulmozhi, N., Aranzales, D. & Koper, M. T. M. Double layer at the Pt(111)–aqueous electrolyte interface: potential of zero charge and anomalous Gouy–Chapman screening. *Angew. Chem. Int. Ed.* **59**, 711–715 (2020).
4. Ojha, K., Doblhoff-Dier, K. & Koper, M. T. M. Double-layer structure of the Pt(111)–aqueous electrolyte interface. *Proc. Natl Acad. Sci. USA* **119**, 3 (2022).
5. Doblhoff-Dier, K. & Koper, M. T. M. Modeling the Gouy–Chapman diffuse capacitance with attractive ion-surface interaction. *J. Phys. Chem. C* **125**, 16664–16673 (2021).
6. Le, J.-B., Fan, Q.-Y., Li, J.-Q. & Cheng, J. Molecular origin of negative component of Helmholtz capacitance at electrified Pt(111)/water interface. *Sci. Adv.* **6**, eabb1219 (2020).
7. Nong, H. N. et al. Key role of chemistry versus bias in electrocatalytic oxygen evolution. *Nature* **587**, 408–413 (2020).
8. Grimaud, A. et al. Activating lattice oxygen redox reactions in metal oxides to catalyse oxygen evolution. *Nat. Chem.* **9**, 457–465 (2017).
9. Oener, S. Z., Bergmann, A. & Roldan Cuenya, B. Designing active oxides for a durable oxygen evolution reaction. *Nat. Synth.* **2**, 817–827 (2023).
10. Haase, F. T. et al. Size effects and active state formation of cobalt oxide nanoparticles during the oxygen evolution reaction. *Nat. Energy* **7**, 765–773 (2022).
11. Schlögl, R. Heterogeneous catalysis. *Angew. Chem. Int. Ed.* **54**, 3465–3520 (2015).
12. Pfeifer, V. et al. Reactive oxygen species in iridium-based OER catalysts. *Chem. Sci.* **7**, 6791–6795 (2016).
13. Pfeifer, V. et al. In situ observation of reactive oxygen species forming on oxygen-evolving iridium surfaces. *Chem. Sci.* **8**, 2143–2149 (2017).
14. Gonella, G. et al. Water at charged interfaces. *Nat. Rev. Chem.* **5**, 466–485 (2021).
15. Oener, S. Z., Foster, M. J. & Boettcher, S. W. Accelerating water dissociation in bipolar membranes and for electrocatalysis. *Science* **369**, 1099–1103 (2020).
16. Seeberger, D., McLaughlin, D., Hauenstein, P. & Thiele, S. Bipolar-interface fuel cells—an underestimated membrane electrode assembly concept for PGM-free ORR catalysts. *Sustain. Energy Fuels* **4**, 2508–2518 (2020).
17. Mayerhöfer, B. et al. Bipolar membrane electrode assemblies for water electrolysis. *ACS Appl. Energy Mater.* **3**, 9635–9644 (2020).
18. Oener, S. Z., Twight, L. P., Lindquist, G. A. & Boettcher, S. W. Thin cation-exchange layers enable high-current-density bipolar membrane electrolyzers via improved water transport. *ACS Energy Lett.* **6**, 1–8 (2021).
19. Vermaas, D. A. & Smith, W. A. Synergistic electrochemical CO_2 reduction and water oxidation with a bipolar membrane. *ACS Energy Lett.* **1**, 1143–1148 (2016).
20. Digdaya, I. A. et al. A direct coupled electrochemical system for capture and conversion of CO_2 from oceanwater. *Nat. Commun.* **11**, 4412 (2020).
21. Eisaman, M. D. et al. CO_2 separation using bipolar membrane electrodialysis. *Energy Environ. Sci.* **4**, 1319–1328 (2011).
22. Frilette, V. J. Preparation and characterization of bipolar ion exchange membranes. *J. Phys. Chem.* **60**, 435–439 (1956).
23. Mitchell, J. B., Chen, L., Langworthy, K., Fabrizio, K. & Boettcher, S. W. Catalytic proton–hydroxide recombination for forward-bias bipolar membranes. *ACS Energy Lett.* **7**, 3967–3973 (2022).
24. Strathmann, H., Krol, J., Rapp, H.-J. & Eigenberger, G. Limiting current density and water dissociation in bipolar membranes. *J. Memb. Sci.* **125**, 123–142 (1997).
25. Laidler, K. J. & King, M. C. Development of transition-state theory. *J. Phys. Chem.* **87**, 2657–2664 (1983).
26. He, Z., Chen, Y., Santos, E. & Schmickler, W. The pre-exponential factor in electrochemistry. *Angew. Chem. Int. Ed.* **57**, 7948–7956 (2018).
27. Liu, L. & Guo, Q. X. Isokinetic relationship, isoequilibrium relationship, and enthalpy–entropy compensation. *Chem. Rev.* **101**, 673–695 (2001).
28. Teschner, D. et al. In situ surface coverage analysis of RuO_2-catalysed HCl oxidation reveals the entropic origin of compensation in heterogeneous catalysis. *Nat. Chem.* **4**, 739–745 (2012).
29. Kosmulski, M. *Surface Charging and Points of Zero Charge* https://doi.org/10.1201/9781420051896 (CRC Press, 2009).
30. Ledezma-Yanez, I. et al. Interfacial water reorganization as a pH-dependent descriptor of the hydrogen evolution rate on platinum electrodes. *Nat. Energy* **2**, 17031 (2017).
31. Garcia-Araez, N., Climent, V. & Feliu, J. Potential-dependent water orientation on Pt(111), Pt(100), and Pt(110), as inferred from laser-pulsed experiments. Electrostatic and chemical effects. *J. Phys. Chem. C* **113**, 9290–9304 (2009).
32. Climent, V., Coles, B. A. & Compton, R. G. Laser-induced potential transients on a Au(111) single-crystal electrode. Determination of the potential of maximum entropy of double-layer formation. *J. Phys. Chem. B* **106**, 5258–5265 (2002).
33. Chen, L., Xu, Q. & Boettcher, S. W. Kinetics and mechanism of heterogeneous voltage-driven water-dissociation catalysis. *Joule* https://doi.org/10.1016/j.joule.2023.06.011 (2023).
34. Bligaard, T. et al. On the compensation effect in heterogeneous catalysis. *J. Phys. Chem. B* **107**, 9325–9331 (2003).
35. Oener, S. Z., Ardo, S. & Boettcher, S. W. Ionic processes in water electrolysis: the role of ion-selective membranes. *ACS Energy Lett.* **2**, 2625–2634 (2017).
36. Eigen, M. & Maeyer De, L. Self-dissociation and protonic charge transport in water and ice. *Proc. R. Soc. London Ser. A* **247**, 505–533 (1958).

37. Lazanas, A. C. & Prodromidis, M. I. Electrochemical impedance spectroscopy—a tutorial. *ACS Meas. Sci. Au* **3**, 162–193 (2023).

38. Wang, S. et al. Electrochemical impedance spectroscopy. *Nat. Rev. Methods Primers* **1**, 41 (2021).

39. Taberna, P. L., Simon, P. & Fauvarque, J. F. Electrochemical characteristics and impedance spectroscopy studies of carbon–carbon supercapacitors. *J. Electrochem. Soc.* **150**, A292 (2003).

40. Yang, B. et al. Engineering relaxors by entropy for high energy storage performance. *Nat. Energy* https://doi.org/10.1038/s41560-023-01300-0 (2023).

41. Bockris, J. O., Mehl, W., Conway, B. E. & Young, L. Frequency variation of the capacity and resistance of the electrical double layer at a metal–solution interface. *J. Chem. Phys.* **25**, 776–777 (1956).

42. Conway, B. E., Tessier, D. F. & Wilkinson, D. P. Experimental evidence for the potential-dependence of entropy of activation in electrochemical reactions in relations to the temperature-dependence of tafel slopes. *J. Electroanal. Chem. Interfacial Electrochem.* **199**, 249–269 (1986).

43. Conway, B. E., Phillips, Y. & Qian, S. Y. Surface electrochemistry and kinetics of anodic bromine formation at platinum. *J. Chem. Soc. Faraday Trans.* **91**, 283–293 (1995).

44. Tang, B. Y., Bisbey, R. P., Lodaya, K. M., Toh, W. L. & Surendranath, Y. Reaction environment impacts charge transfer but not chemical reaction steps in hydrogen evolution catalysis. *Nat. Catal.* **6**, 339–350 (2023).

45. Monteiro, M. C. O., Goyal, A., Moerland, P. & Koper, M. T. M. Understanding cation trends for hydrogen evolution on platinum and gold electrodes in alkaline media. *ACS Catal.* **11**, 14328–14335 (2021).

46. Bender, J. T. et al. Understanding cation effects on the hydrogen evolution reaction. *ACS Energy Lett.* **8**, 657–665 (2023).

47. Narangoda, P., Spanos, I., Masa, J., Schlögl, R. & Zeradjanin, A. R. Electrocatalysis beyond 2020: how to tune the preexponential frequency factor. *ChemElectroChem* **9**, e202101278 (2022).

48. Zeradjanin, A. R., Narangoda, P., Masa, J. & Schlögl, R. What controls activity trends of electrocatalytic hydrogen evolution reaction? Activation energy versus frequency factor. *ACS Catal.* **19**, 11597–11605 (2022).

49. Westendorff, K. S., Hülsey, M. J., Wesley, T. S., Roman-Leshkov, Y. & Surendranath, Y. Electrically driven proton transfer promotes Brønsted acid catalysis by orders of magnitude. *Science* **383**, 757–763 (2024).

50. Morelli, A. M., Ravera, S., Calzia, D. & Panfoli, I. An update of the chemiosmotic theory as suggested by possible proton currents inside the coupling membrane. *Open Biol.* **9**, 180221 (2019).

51. Tributsch, H. Light driven proton pumps. *Ion. (Kiel.)* **6**, 161–171 (2000).

52. Weifu Lee, J. Proton-electrostatics hypothesis for localized proton coupling bioenergetics. *Bioenerg. Open Access* **1**, 104 (2012).

53. Saeed, H. A. & Lee, J. W. Experimental demonstration of localized excess protons at a water membrane interface. *Bioenerg. Open Access* **4**, 127 (2015).

54. Elston, T., Wang, H. & Oster, G. Energy transduction in ATP synthase. *Nature* **391**, 510–513 (1998).

55. Eigen, M. Kinetics of proton transfer processes. *Discuss. Faraday Soc.* **39**, 7–15 (1965).

56. Zheng, C. et al. A two-directional vibrational probe reveals different electric field orientations in solution and an enzyme active site. *Nat. Chem.* **14**, 891–897 (2022).

57. Fried, S. D., Bagchi, S. & Boxer, S. G. Extreme electric fields power catalysis in the active site of ketosteroid isomerase. *Science* **346**, 1510–1514 (2014).

58. Bui, J. C., Corpus, K. R. M., Bell, A. T. & Weber, A. Z. On the nature of field-enhanced water dissociation in bipolar membranes. *J. Phys. Chem. C* **125**, 24974–24987 (2021).

59. Eberhardt, D., Santos, E. & Schmickler, W. Hydrogen evolution on silver single crystal electrodes—first results. *J. Electroanal. Chem.* **461**, 76–79 (1999).

60. Tang, Z. Q., Liao, L. W., Zheng, Y. L., Kang, J. & Chen, Y. X. Temperature effect on hydrogen evolution reaction at Au electrode. *Chin. J. Chem. Phys.* **25**, 469–474 (2012).

Author contributions

S.Z.O. conceived the project. C.G.R. performed the temperature-dependent studies on the BPM fuel cell with assistance from J.M.G.-G. F.S. and S.Z.O. performed the temperature-dependent electrocatalysis studies. C.G.R. performed the multiphysics simulations. C.G.R. and S.Z.O. analysed the data and discussed them with B.R.C. C.G.R. and S.Z.O. wrote the paper with the help of B.R.C.

Competing interests

The authors declare no competing interests.

Additional information

Supplementary information The online version contains supplementary material available at https://doi.org/10.1038/s41560-024-01484-z.

Correspondence and requests for materials should be addressed to Sebastian Z. Oener.

Peer review information *Nature Energy* thanks the anonymous reviewers for their contribution to the peer review of this work.

Reprints and permissions information is available at www.nature.com/reprints.

Publisher's note Springer Nature remains neutral with regard to jurisdictional claims in published maps and institutional affiliations.